Synergistic enhancement of electrocatalytic CO₂ reduction to C₂ oxygenates at nitrogen-doped nanodiamonds/Cu interface

Hongxia Wang [1,2,8], Yan-Kai Tzeng[3,8], Yongfei Ji[4,8], Yanbin Li[1], Jun Li[1], Xueli Zheng [1], Ankun Yang [1], Yayuan Liu [1], Yongji Gong[1], Lili Cai[1], Yuzhang Li [1], Xiaokun Zhang[1], Wei Chen[1], Bofei Liu[1], Haiyu Lu[3], Nicholas A. Melosh [1,5], Zhi-Xun Shen [3,5], Karen Chan [4]*, Tianwei Tan[2,6]*, Steven Chu[3,7]* and Yi Cui [1,5]*

To date, effective control over the electrochemical reduction of CO₂ to multicarbon products (C ≥ 2) has been very challenging. Here, we report a design principle for the creation of a selective yet robust catalytic interface for heterogeneous electrocatalysts in the reduction of CO₂ to C₂ oxygenates, demonstrated by rational tuning of an assembly of nitrogen-doped nanodiamonds and copper nanoparticles. The catalyst exhibits a Faradaic efficiency of ~63% towards C₂ oxygenates at applied potentials of only −0.5 V versus reversible hydrogen electrode. Moreover, this catalyst shows an unprecedented persistent catalytic performance up to 120 h, with steady current and only 19% activity decay. Density functional theory calculations show that CO binding is strengthened at the copper/nanodiamond interface, suppressing CO desorption and promoting C₂ production by lowering the apparent barrier for CO dimerization. The inherent compositional and electronic tunability of the catalyst assembly offers an unrivalled degree of control over the catalytic interface, and thereby the reaction energetics and kinetics.

Novel catalysts for carbon-neutral energy conversion processes are essential to address climate change and the rising global energy demand[1,2]. The development of catalysts for reduction of carbon dioxide (CO₂) as a route towards the storage of intermittent renewable energy sources is particularly appealing[3–5]. Electrolytic approaches benefit from using an aqueous medium, which is cheap, abundant and environmentally benign, and typically can be operated under ambient temperature and pressure[6]. Known electrocatalysts employed in CO₂ reduction reactions are precious metals[7–9], base metals[10–12], metal oxides[13], metal dichalcogenides[14], molecular catalysts[14,15], covalent organic frameworks[16,17] and metal organic frameworks[18,19]. Nevertheless, many impediments to scalability and ultimate implementation of these catalysts[20,21] remain, such as low energetic efficiency, poor selectivity for the desired products, high cost and inadequate electrochemical stability.

Of the prevalent CO₂ electrocatalysts, most primarily generate carbon monoxide (CO)[22–24] or formic acid (HCOOH)[12]. Only recently have advanced catalysts capable of producing C ≥ 2 products in neutral aqueous media been reported[25–28]. Nonetheless, nearly all of these reductive transformations are processed at very negative applied potentials (−0.9 V versus reversible hydrogen electrode (RHE), or more negative), most suffer from low to moderate yields for multicarbon products and long-term electrochemical durability remains a big problem (typically less than 40 h). Of particular interest, is the earth-abundant metal Cu, which is capable of converting CO₂ to a range of reduced C ≥ 2 products[29,30], but is

usually accompanied by catalyst durability issues under electrochemical conditions. Against this background, we seek to explore the synergistic effect originating from the interface between Cu and a second electroactive component, by rational tuning of the catalyst assembly to trigger production of multicarbon products, whilst improving the electrochemical stability at the catalytic interface, which is not owned by the parent Cu. In particular, we have chosen nitrogen-doped nanodiamond as the second component to construct the desired catalytic interface, due to its low cost relative to precious metal catalysts, high electroactivity, high surface area and, very importantly, its excellent chemical stability[31,32]. Moreover, N-doped nanodiamond contains a dominant N-*sp*³C component[32], which has been shown to be critical for superior performance in electrocatalysis[33]. We anticipate that the constructed material assembly offers extensive compositional and electronic tunability at the interface for binding of the key C₁ intermediates, as well as for their reaction energetics. As such, we hypothesize that the feasibility of C–C bond formation between these intermediates can therefore be greatly improved and subsequent reaction pathways, unlike for the sole parent catalytic component, would be strongly expected to fulfil the desired aim of production of C₂ oxygenates.

Preparation and electrochemical performance of ND and N-ND
Nitrogen-doped nanodiamond films were synthesized by carrying out microwave plasma-enhanced chemical vapour deposition

¹Department of Materials Science and Engineering, Stanford University, Stanford, CA, USA. ²Beijing Advanced Innovation Center for Soft Matter Science and Engineering, Beijing University of Chemical Technology, Beijing, China. ³Department of Physics, Stanford University, Stanford, CA, USA. ⁴SUNCAT Center for Interface Science and Catalysis, SLAC National Accelerator Laboratory, Menlo Park, CA, USA. ⁵Stanford Institute for Materials and Energy Science, SLAC National Accelerator Laboratory, Menlo Park, CA, USA. ⁶National Energy R&D Center for Biorefinery, Beijing University of Chemical Technology, Beijing, China. ⁷Department of Molecular and Cellular Physiology, Stanford University, Stanford, CA, USA. ⁸These authors contributed equally: Hongxia Wang, Yan-Kai Tzeng, Yongfei Ji. *e-mail: kchan@fysik.dtu.dk; twtan@mail.buct.edu.cn; schu@stanford.edu; yicui@stanford.edu
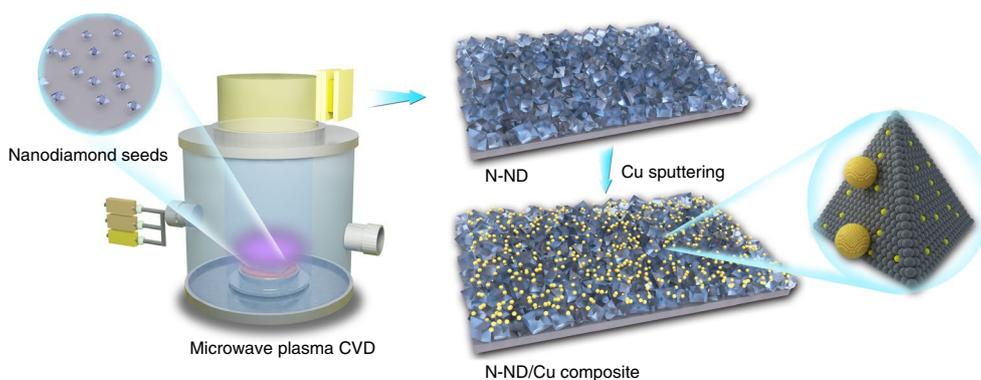
Fig. 1 | Preparation of composite materials. A schematic illustration of preparation of N-ND and N-ND/Cu composite materials.

(CVD) on a nanodiamond seed, prefunctionalized silicon wafer substrate (Fig. 1, details in Methods). The nitrogen-doping level was modulated by tuning the N_2 flow rate from 0 to 25 standard cubic centimeters per minute (sccm), whereas that of the CH_4 and H_2 was maintained at 10 and 300 sccm, respectively. The optimized N-doped nanodiamond/Si material under a N_2 flow rate of 15 sccm and ~0.2 atom% is denoted as N-ND, and nanodiamond/Si without N doping is referred to as ND. Further sputtering of Cu onto the as-prepared N-ND film results in the desired N-ND/Cu composite. Likewise, the amount of incorporated Cu can be tuned by changing the sputtering time (0–60 s). The resultant composite with 30 s of Cu sputtering is denoted as N-ND/Cu.

We used scanning electron microscopy (SEM) to identify the surface morphology of the ND and N-ND films. A distinct morphological pattern for N-ND (Fig. 2a), different from that for ND (Supplementary Fig. 1), is evidenced on nitrogen doping, as the diamond particle density decreases by one magnitude to 10^9 cm^{-2}, whereas the particle size shrinks by 15-fold to 20 nm. We then used a focused ion beam (FIB) to cut through the film and explore the interfacial structure between the film and the substrate, and a thickness of 1.7 μm for the N-ND film was thereby determined (Fig. 2b). The averaged microscopic roughness of the ND and N-ND films was studied by atomic force microscopy (AFM). Clearly, the significantly smaller microscopic roughness value (denoted as R_a) of 11.91 nm in N-ND (Supplementary Fig. 2b), compared with 34.32 nm for ND (Supplementary Fig. 2a) reveals a smoother surface in the N-ND film. Raman spectroscopy was probed to elucidate the structural bonding of the N-ND film (Fig. 2c). A unique feature of nanodiamonds is the peak centred at ~1,180 cm^{-1}, which represents nanodiamond crystallites (Supplementary Fig. 3).

The chemical environment of nitrogen species and their fractional content in the host lattice have a critical effect on the electrocatalytic performance of N-doped carbon materials[34,35]. Thus, we performed an X-ray photoelectron spectroscopy (XPS) study (Fig. 2d), in combination with secondary ion mass spectrometry (SIMS) to acquire the atomic configuration and stoichiometric composition of N-ND. The N-ND contains three elements, C, N and O, and the total nitrogen mass content is approximately 0.3 atom% (Supplementary Fig. 4). The high-resolution N 1s spectrum has been deconvoluted into sub-peaks at approximately 398.5, 400.2 and 402.6 eV in Fig. 2d, revealing three types of nitrogen configurations: N-sp^3C with the strongest presence, N-sp^2C and N–O (ref. [36]). Consequently, we anticipate that N-ND/Cu may exhibit superior CO_2 activity compared with carbon materials that use N-sp^2C as the catalytically active component[35]. The greatly improved electrocatalytic activity of N-sp^3C compared with N-sp^2C has been previously verified[33].

Linear sweep voltammetry (LSV) of the N-ND electrode in 0.5 M CO_2-saturated $KHCO_3$ (pH 7.3) reveals a large improvement in catalytic activity relative to nitrogen-free ND (Supplementary Fig. 5a).

All of the as-synthesized N-ND electrodes with different nitrogen content deliver significantly more current than ND (Supplementary Fig. 5b). The current enhancement observed in N-ND decreases slightly in the absence of CO_2, suggesting that the excess current drives the CO_2 reduction (Supplementary Fig. 6a). Controlled potential electrolysis experiments were carried out to identify and quantify the reduced products. Liquid products were analysed by ^{1}H-NMR (Supplementary Fig. 7), whereas gaseous products were quantified by gas chromatography (GC). In the potential window examined, from −1.2 to −1.5 V, only less than 10% of Faradaic efficiencies (FEs) are attributed to formate production in the ND case (Fig. 2e and Supplementary Fig. 8) and the majority of the total current has been consumed for H_2 formation (Supplementary Fig. 9). In contrast, N-ND enables reduction of CO_2 to generate a decent amount of formate and minimal acetate, along with reasonable yields (Fig. 2e). In particular, total CO_2 selectivity was significantly improved for the N-ND electrode, with enhanced production rate (Fig. 2f) and suppressed H_2 production (Supplementary Fig. 10) together leading to FE values exceeding 45%, which is as much as 30% higher than those of the ND electrode at all potentials. What is surprising is the formation of acetate. Although the amount of acetate formed is not significant (7.9%), this is still rare for nitrogen-doped carbon materials in electrochemical CO_2 reduction.

Preparation and electrochemical performance of N-ND/Cu

Further sputtering of Cu onto the surface of the as-synthesized N-ND does not alter the morphology of nanodiamonds, as reflected by the nearly identical SEM and AFM images for N-ND/Cu (Supplementary Figs. 1b and 2c) and N-ND (Fig. 2a and Supplementary Fig. 2b). High-resolution transmission electron microscopy (HRTEM) suggests direct interfacial contact between N-ND and Cu (Fig. 3a), which is consistent with previous observations on the Cu and N-doped carbon nanomaterials interface[37,38]. The distinct diffraction rings have lattice spacings of 1.96 and 2.10 Å indexed to the Cu(111) and nanodiamond(111) reflections, which have been confirmed. Transmission electron microscope (TEM) images show that the Cu nanoparticles (CuNPs) have sizes around 3 nm. To gain compositional information for the N-ND/Cu film, we then performed a scanning transmission electron microscope (STEM) study combined with elemental mapping using energy dispersive X-ray spectroscopy (EDX) (Fig. 3b and Supplementary Fig. 11) to investigate the cross-section of the sample. In the upper left-hand quadrant of Fig. 3b, the upper dark area is the diamond film and the brighter lower half shows the location of Cu as revealed by the EDX signal. On the other hand, the EDX signal shows that the carbon distribution penetrates into the Cu region. The low Cu concentration on the N-ND substrate surface was further identified by XPS characterization (Supplementary Fig. 12). We used two-dimensional (2D) grazing-incidence wide-angle X-ray
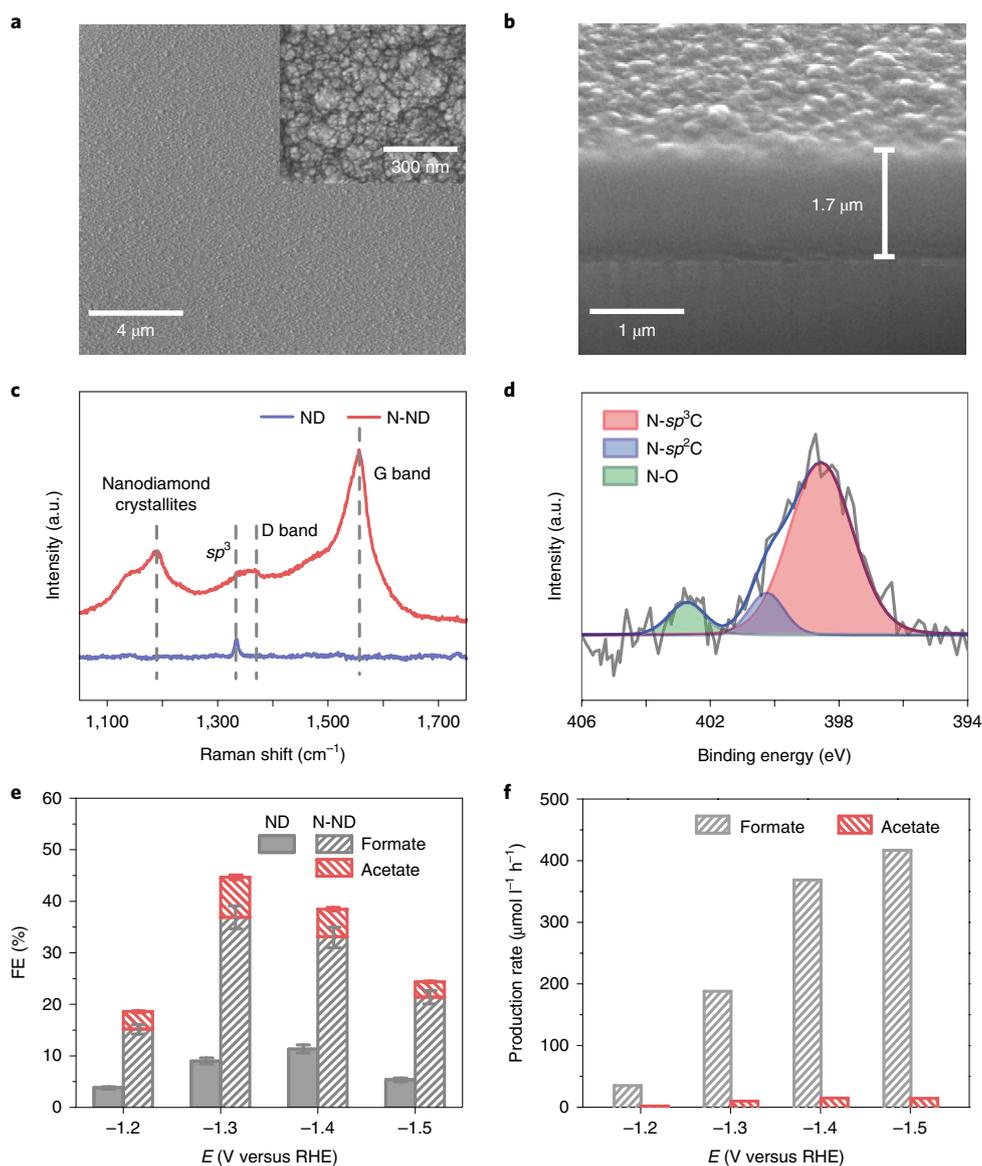
Fig. 2 | Structural, configurational and electrochemical characterization of ND and N-ND electrode materials. a, Low-magnification SEM image of as-synthesized N-ND. Inset: the corresponding high-magnification pattern. **b**, FIB image of N-ND film with a tilt of 52° to study the cross-section. The scale is divided by cos(52°) to give the real thickness. **c**, Raman spectrum of N-ND. **d**, High-resolution N 1s XPS spectrum of the N-ND, deconvoluted into three subpeaks representing the chemical environment of N-sp^3C (N atom bonds to sp^3-hybridized C atom), N-sp^2C (N atom bonds to sp^2-hybridized C atom) and N–O. **e**, FEs for acetate and formate ion production as a function of applied potentials for N-ND (0.2 atom% doping) electrodes. FEs for formate formation for ND electrodes are plotted as reference. Controlled potential electrolysis was performed in 0.5 M aqueous $KHCO_3$ saturated with CO_2 (pH 7.3). The error bars represent the standard deviation of three independent samples. **f**, Production rates of acetate and formate as a function of applied potentials for N-ND electrodes.

scattering (GIWAXS) to explore global orientation and crystallinity of the N-ND/Cu film. The out-of-plane reflection halos centred at $q_y = 3.04\,\text{Å}^{-1}$ (indexed as Cu(111)) and $q_y = 3.07\,\text{Å}^{-1}$ (indexed as nanodiamond(111)) are largely overlapped and can also be converted into a particular X-ray diffraction pattern (Fig. 3c). The X-ray diffraction pattern displays four peaks at the expected diffraction angles for metallic Cu ($2\theta = 43.7$ and 50.3, indexed to Cu(111) and Cu(200)), nanodiamond ($2\theta = 44.2$, indexed to nanodiamond(111)) and a very small copper oxide peak ($2\theta = 36.4$, indexed to Cu_2O(111)) due to exposure to air (Supplementary Figs. 13 and 14). To better evaluate the contribution of the N-ND substrate to the change of chemical state and bonding of the surface Cu species, we carried out an extended X-ray absorption fine

structure (EXAFS) study on N-ND/Cu. The Cu K-edge EXAFS spectrum (Supplementary Fig. 15) shows the presence of metallic Cu and copper oxide in the as-prepared samples[29]. It is worth noting that metallic Cu–Cu (Cu⁰) character dominates in comparison with ND/Cu and Cu nanoparticles, where the metallic copper is usually believed to be the active species throughout a test catalytic period[39].

The electrocatalytic performance of N-ND/Cu (Fig. 3d–h) was found to be strikingly different from that of N-ND (Fig. 2e,f). Controlled potential electrolysis experiments over a potential range of −0.7 to −0.4 V further underline the synergy between the two components. An improved CO_2 reduction performance is revealed by both the significantly enhanced total FEs (Fig. 3d) and the production rates (Fig. 3f), whereas the N-ND electrode shows no CO_2
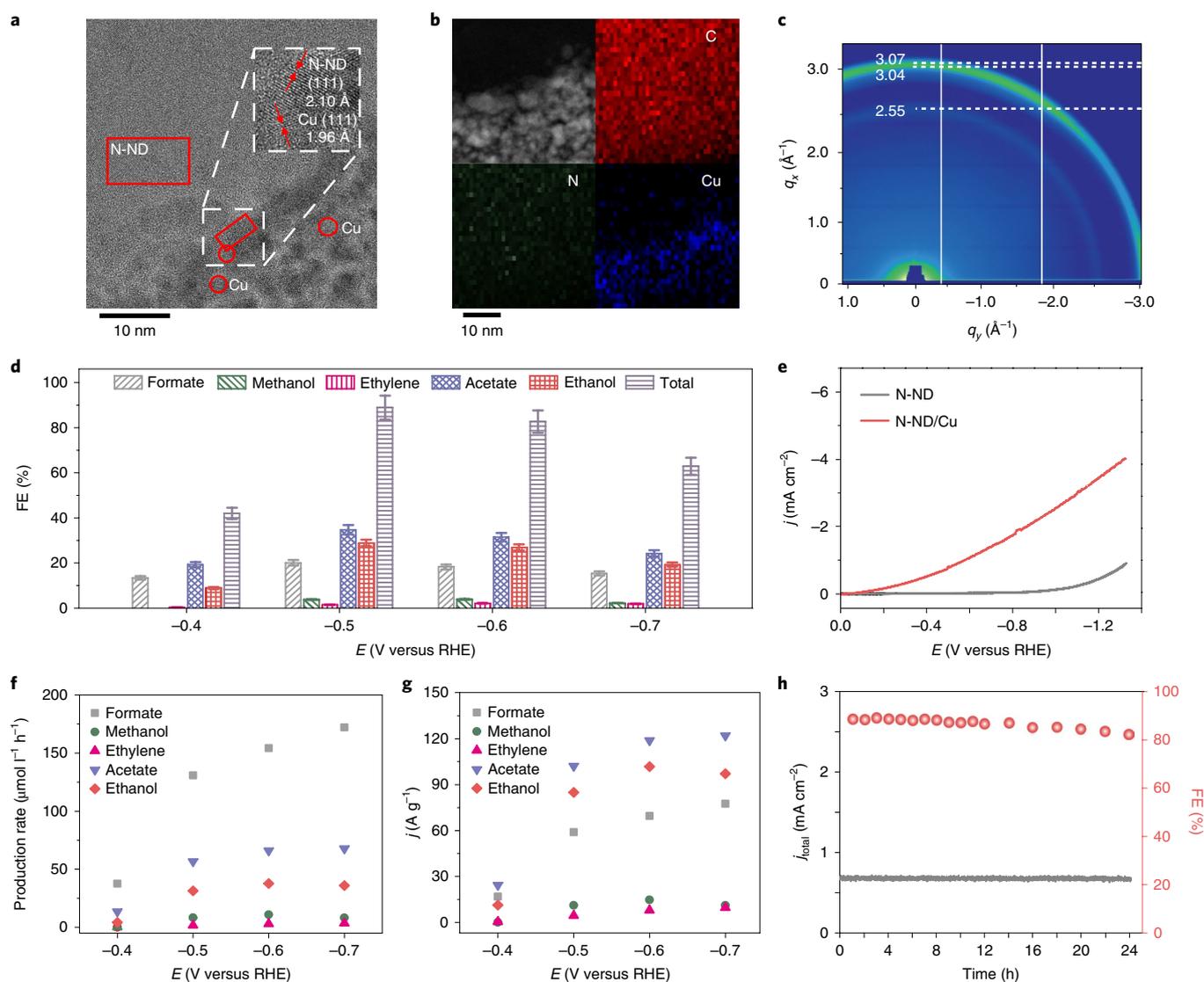
Fig. 3 | Structural, configurational and electrochemical characterization of N-ND/Cu electrode materials. a, HRTEM image of N-ND/Cu. The HRTEM image shows the presence of both Cu and nanodiamond as confirmed by lattice fringes of the selected regions in the micrograph. **b**, STEM image (top left) and corresponding EDX spectroscopy elemental mapping (C, N and Cu) of N-ND/Cu. **c**, GIWAXS 2D pattern of N-ND/Cu film. The weak out-of-plane reflection arc was also observed at $q = 2.55\,\text{Å}^{-1}$, which is indexed to the $Cu_2O(111)$ reflection, due to exposure to air. **d**, FE values for formate, methanol, ethylene, acetate and ethanol production by N-ND/Cu electrodes, with the remaining current going to H_2 production. Electrolysis was performed at potentials from -0.4 to $-0.7\,\text{V}$ (versus RHE). The error bars represent the standard deviation of three independent samples. **e**, LSV of the electrodes of N-ND/Cu and N-ND in 0.5 M CO_2-saturated $KHCO_3$ (pH 7.3) (scan rate of 50 mV s^{-1}). **f**, Production rates for formate, methanol, ethylene, acetate and ethanol production by N-ND/Cu electrodes. **g**, Mass activity (ampere per gram of Cu) of acetate and ethanol by N-ND/Cu electrodes. **h**, Total FEs (red balls) of all reduced carbon-based products and total current density (grey line) of N-ND/Cu electrodes over a long-term bulk electrolysis. Both current density and FE show a slight decline during a 24-h period of controlled potential electrolysis at $-0.5\,\text{V}$ (versus RHE).

activity in the same test range (Fig. 2e,f). For N-ND/Cu at the optimal applied potential of $-0.5\,\text{V}$, the total FE of CO_2 reduction is up to 89.0% (Fig. 3d) and the total mass activity exceeds 261.6 A g^{-1} (ampere per gram of Cu, Fig. 3g). Compared to the N-ND reference, N-ND/Cu has a significantly positive shift in onset potential ($-0.17\,\text{V}$ versus RHE) (Fig. 3e and Supplementary Fig. 5c), suggesting that the catalytic environment created by Cu incorporation drastically lowers the required overpotential for CO_2 reduction on the parent N-ND. In contrast, the current enhancement for N-ND/Cu disappears under an Ar atmosphere (Supplementary Fig. 6b). We therefore postulate that the increased current that drives excess CO_2 reduction might be a consequence of synergy between nitrogen doping and incorporated Cu. This conjecture is also consistent

with the fact that electrodes fabricated by sputtering Cu onto nanodiamond without nitrogen doping, namely ND/Cu, deliver minimal current under the same conditions (Supplementary Fig. 16a).

Another striking observation is the altered product distribution with respect to N-ND: a significant amount of acetate and ethanol as well as a small amount of ethylene is produced. In particular, the FE$_{acetate}$ of 34.7% and FE$_{ethanol}$ of 28.9% have been quantified (Fig. 3d and Supplementary Fig. 17a), along with determination of a production rate of 56.7 µmol l^{-1} h^{-1} for acetate and 31.4 µmol l^{-1} h^{-1} for ethanol formation (Fig. 3f). It should be emphasized that the unprecedented Cu mass activity for acetate and ethanol production, 102.2 and 84.9 A g^{-1} at $-0.5\,\text{V}$ (equivalent to 420 mV overpotential) (Fig. 3g), respectively, represents one of the most effective electrocatalysts

that can reduce CO_2 to C_2 oxygenates (Supplementary Table 1). The improved catalytic performance is mostly retained throughout long-term bulk electrolysis. With an applied potential of −0.5 V, N-ND/Cu can continuously produce more than 686.0 mg of acetate and 291.6 mg of ethanol per milligram of Cu during a 24-h time course (20 ml volume) (Supplementary Fig. 18), with a steady current density and almost retained high total FE (>80%) (Fig. 3h). More intriguing is that N-ND/Cu shows unprecedented persistent catalytic performance up to 120 h with a steady current and only 19% activity decay (Supplementary Fig. 19a). Clearly, N-ND/Cu is an electrode that is far superior to CuNP and N-ND in terms of both selectivity and electrochemical stability (Supplementary Fig. 19b). At this applied potential, the formation of acetate and ethanol is unlikely due to Cannizzaro disproportionation[40], whereas the selectivity of H_2 production is relatively low at less negatively applied potentials, but the hydrogen evolution reaction is not fully inhibited. However, the production rate of H_2 increases dramatically along with the more negative potential (Supplementary Fig. 20).

We hypothesize that the improved electrochemical durability in N-ND/Cu is due to a synergistic stabilization of the catalytic interface. Double-layer capacitance measurements before and immediately after bulk electrolysis show the change in the electrocatalytically active surface area (ECSA)[41], which closely associates with catalytic activity of CO_2 reduction[28]. We therefore carried out double-layer capacitance measurements on both N-ND/Cu and reference CuNP (by direct sputtering CuNPs on a silicon substrate, Methods) electrodes to provide a quantitative measure of the ECSA. The CuNP electrode rapidly loses significant active surface area and only 31% of the original ECSA remains after 24 h of electrolysis (Supplementary Fig. 21a). Such a deactivation pathway has been previously rationalized as the coalescence of metal nanoparticles to form larger aggregates[17], consistent with our SEM observations on CuNP post-electrolysis (Supplementary Fig. 22). In contrast, N-ND/Cu can effectively prevent particle coalescence and thereby minimize the deactivation of activity. In particular, N-ND/Cu loses only 8% of its original ECSA following 24-h bulk electrolysis (Supplementary Fig. 21b). Additional evidence of N-ND/Cu electrode durability comes from material characterizations of N-ND/Cu immediately after long-term electrolysis. All SEM and GIWAXS studies reveal the same characteristic features as the N-ND/Cu electrode prior to electrolysis experiments (Supplementary Figs. 1c, 12c, 13d, and 23).

Density functional theory calculations

In addition to the synergistic effect in stabilization of the N-ND/Cu interface, we investigated the origin of the improved catalytic activity and altered selectivity in CO_2 reduction. We initially thought that incorporation of Cu onto N-ND would enlarge the accessible active surface area, comparable with increasing the number of active sites, and lead to improved catalytic performance. To test this hypothesis, we performed double-layer capacitance measurements for both N-ND/Cu and N-ND (Supplementary Fig. 21b,c), but, contrary to expectations, the formation of the N-ND/Cu interface slightly reduced the original ECSA, from a capacitance of 37.6 μF to one of 32.4 μF.

To further investigate the origins of the high activity and selectivity of our composite materials, the reaction energetics of various surfaces were analysed using density functional theory (DFT) calculations (details in Methods and Supplementary information). Figure 4a and Supplementary Fig. 24 show the free energies of the bare and H* covered diamond surfaces as a function of the chemical potential of H:

$$\Delta\mu_H = \frac{1}{2}k_B T \ln\frac{p_{H_2}}{p_{H_2}^o} \tag{1}$$

In general, the bare ND(111) surface is very reactive; it can be stabilized by the adsorption of H*, but the H*-saturated surface does not interact with CO_2. The binding free energy of H* on the diamond surface is −1.98 eV at standard conditions of $\Delta\mu_H = 0$ and $p_{H_2} = 1$ bar. Under reducing conditions, the H* would be further stabilized, making it highly energetically unfavourable for adsorbates to interact with the surface. This is consistent with the experimental observation of low activity of the ND electrode. In addition, the low conductivity of ND may also limit its overall electrocatalytic activity, as low conductivity usually associates with a low current density, which is a crucial metric for electrocatalyst evaluation[35].

The DFT calculation shows that nitrogen substitution into diamond favours the formation of formate. The difference in the substitution energy for nitrogen for the most stable surface and subsurface sites was small, ~0.12 eV (Supplementary Table 2), which suggests that it is likely that there is a distribution of sites near the surface of N-ND where N is present. Nitrogen substitution at the outermost C atoms does not give facile CO_2R reaction energetics (Supplementary Fig. 25), but the N substitution of the subsurface C significantly lowers the thermochemical barrier for reducing CO_2 to formate (Fig. 4b). Consequently, a limiting thermodynamic potential of −1.10 V for the reduction of CO_2 to formate is obtained, consistent with the experimental observation that N substitution favours formate production. In addition, the conductivity of diamond can be greatly improved by N substitution; 0.2% N can increase the conductivity by five orders of magnitude[42].

Furthermore, the incorporation of Cu onto the H-terminated surface results in dehydrogenation and formation of a stable ND/Cu and N-ND/Cu interface (Fig. 4a and Supplementary Fig. 26) with an average binding energy of −1.17 eV per Cu–C bond. Copper atoms at the interface appear to be partially oxidized, since Cu donates $0.12e^-$ to diamond, on the basis of Bader charge analysis[43]. Due to the reduction in sigma repulsion[44], the overall CO binding at the interface is strengthened by 0.30 eV compared with that of the Cu(111), which would suppress CO production, as observed experimentally (Supplementary Table 3). The low activity of ND/Cu observed in the experiment may be attributed to its low conductivity, which can be enhanced by nitrogen doping[35]. In addition, the charge transfer from Cu to diamond facilitated by N doping further lowers the CO binding energy by ~0.03–0.10 eV at various doping sites (Supplementary Figs. 27 and 28 and Supplementary Table 3). Previous studies on Cu reveal that the rate-determining step for the formation of C_2 species is the dimerization of CO (ref. [45]) and is pH independent[46]. Furthermore, theoretical studies of the transformation of CO_2 into CO on Cu, suggested as none rate-determining step, have been extensively reported[45,46]. Additional calculations would not provide new insight to complement the current understanding of this process. Given the fact that our primary focus is to elucidate the unique features of the N-ND/Cu interface and correlate them with effective formation of C_2 products, we therefore concentrated on the evaluation of reaction energetics from CO to OCCO dimer, a key intermediate towards C_{2+} product formation[47] (Fig. 4c). At the low coverage limit where adsorbate–adsorbate interactions are negligible, the effective barrier for *OCCO formation from CO(g) on ND/Cu would be the CO dimerization transition state relative to CO(g). This barrier is lower than that corresponding to Cu (Fig. 4d), which would enhance the C_2 activity. This agrees well with the high C_2 activity observed experimentally for N-ND/Cu materials.

The role of C in the Cu/C interface seems to be comparable to that proposed for subsurface O in oxide-derived Cu (ref. [42]), in which the magnitude of the CO binding energy can be increased in the presence of the subsurface O, leading to increased CO coverage and the likelihood of CO–CO coupling[48]. The role of subsurface O in oxide-derived Cu is contentious and in conflict with recent theoretical and experimental investigations of the stability of subsurface oxygen and oxide species under reducing conditions[48,49]. Unlike these examples, the Cu/C interface presented here is kinetically stable due to formation of the strong Cu–C bond. Nitrogen doping
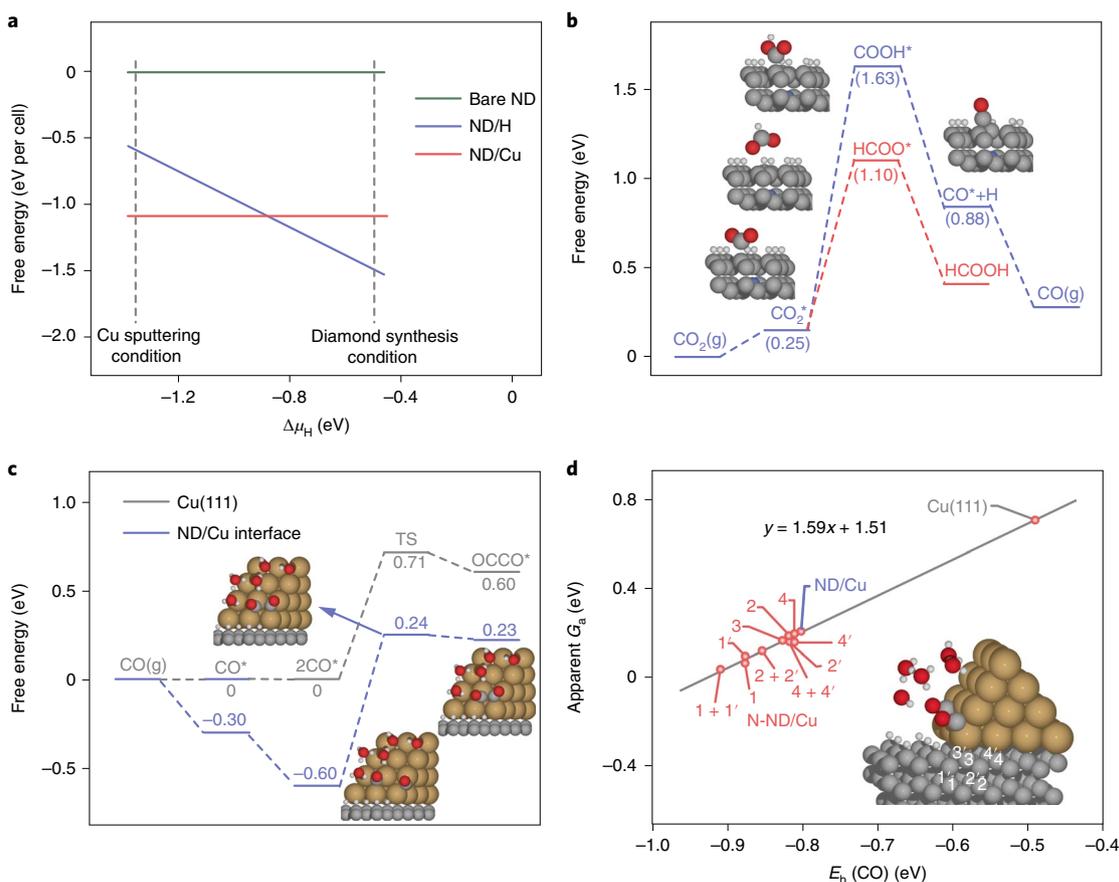
Fig. 4 | DFT calculations. a, Binding free energy of hydrogen (blue) and Cu slabs (red) on bare ND(111) (green) surface as a function of the chemical potential of H, $\Delta\mu_H$. The dashed grey lines denote the $\Delta\mu_H$ under the diamond synthesis condition and Cu sputtering condition. **b**, Free energy diagram for CO_2 reduction reaction to HCOOH (red) and CO (blue) on N-ND(111). **c**, Free energy diagram for CO coupling on the Cu(111) surface (grey) and at the ND/Cu interface (blue). **d**, Scaling relation between the apparent barrier (G_a) and the CO binding energy (E_b) as a function of the location of nitrogen substitution in different locations in the diamond lattice. The data points labelled with X (or X + X') mean that carbon X (or X and X') in the inserted structure model was replaced by N.

is suggested to improve not only the conductivity of the sample, but also the chemical activity of Cu at the interface. Here, the role of the N dopant is neither like the enhancement of CO_2 capture capacity[50], nor solely tuning outer-layer Cu electronic structure to modulate CO_2 activity.

Conclusions

In this paper, we propose a design principle where a catalytic interface can be rationally assembled through incorporation of Cu nanoparticles into N-ND giving rise to N-ND/Cu. According to our investigation, the target CO_2 to C_2 oxygenate transformation indeed occurs at the interface and benefits from the synergy of the two components. At the N-ND/Cu interface the reaction energetics are altered to favour C_{2+} product formation, to give unprecedented high activity and selectivity in comparison with systems reported so far. The catalyst exhibits a FE of ~63% (total CO_2 FE of ~90%) and a production rate of ~90 μmol l⁻¹ h⁻¹ towards C_2 oxygenate (ethanol and acetate) formation at the applied potential of only −0.5 V (versus RHE), at which the parent nitrogen-doped nanodiamonds and Cu nanoparticles display no activity for C_2 oxygenate production. Superior to previous CuNP electrocatalysts applied to CO_2 reduction, N-ND/Cu exhibits a significantly improved catalytic durability of up to 120 h with a steady current and only 19% activity decay. We anticipate that the design principle for this interfaced materials–materials platform will be applicable to a wide range of catalytic

transformations, especially those that require renewable energy input and aqueous compatibility.

Online content

Any methods, additional references, Nature Research reporting summaries, source data, extended data, supplementary information, acknowledgements, peer review information; details of author contributions and competing interests; and statements of data and code availability are available at https://doi.org/10.1038/s41565-019-0603-y.

References

1. Lewis, N. S. & Nocera, D. G. Powering the planet: chemical challenges in solar energy utilization. *Proc. Natl Acad. Sci. USA* **103**, 15729–15735 (2006).
2. Chu, S., Cui, Y. & Liu, N. The path towards sustainable energy. *Nat. Mater.* **16**, 16–22 (2017).
3. Voiry, D., Shin, H. S., Loh, K. P. & Chhowalla, M. Low-dimensional catalysts for hydrogen evolution and CO_2 reduction. *Nat. Rev. Chem.* **1**, 0105 (2018).
4. Liu, C., Colón, B. C., Ziesack, M., Silver, P. A. & Nocera, D. G. Water splitting–biosynthetic system with CO_2 reduction efficiencies exceeding photosynthesis. *Science* **352**, 1210–1213 (2016).
5. Rao, H., Schmidt, L. C., Bonin, J. & Robert, M. Visible-light-driven methane formation from CO_2 with a molecular iron catalyst. *Nature* **548**, 74–77 (2017).

6. Hori, Y. in *Modern Aspects of Electrochemistry* Vol. 42 (eds Vayenas, C. et al.) 89–189 (Springer, 2008).
7. Mariano, R. G., McKelvey, K., White, H. S. & Kanan, M. W. Selective increase in CO₂ electroreduction activity at grain-boundary surface terminations. *Science* **358**, 1187–1192 (2017).
8. Zhu, W. et al. Monodisperse Au nanoparticles for selective electrocatalytic reduction of CO₂ to CO. *J. Am. Chem. Soc.* **135**, 16833–16836 (2013).
9. Gao, D. et al. Size-dependent electrocatalytic reduction of CO₂ over Pd nanoparticles. *J. Am. Chem. Soc.* **137**, 4288–4291 (2015).
10. Gao, S. et al. Partially oxidized atomic cobalt layers for carbon dioxide electroreduction to liquid fuel. *Nature* **529**, 68–71 (2016).
11. Wang, H. et al. Self-selective catalyst synthesis for CO₂ reduction. *Joule* **3**, 1927–1936 (2019).
12. Zhang, S., Kang, P. & Meyer, T. J. Nanostructured tin catalysts for selective electrochemical reduction of carbon dioxide to formate. *J. Am. Chem. Soc.* **136**, 1734–1737 (2014).
13. Gao, D. et al. Enhancing CO₂ electroreduction with the metal–oxide interface. *J. Am. Chem. Soc.* **139**, 5652–5655 (2017).
14. Angamuthu, R., Byers, P., Lutz, M., Spek, A. L. & Bouwman, E. Electrocatalytic CO₂ conversion to oxalate by a copper complex. *Science* **327**, 313–315 (2010).
15. Costentin, C., Drouet, S., Robert, M. & Savéant, J.-M. A local proton source enhances CO₂ electroreduction to CO by a molecular Fe catalyst. *Science* **338**, 90–94 (2012).
16. Lin, S. et al. Covalent organic frameworks comprising cobalt porphyrins for catalytic CO₂ reduction in water. *Science* **349**, 1208–1213 (2015).
17. Diercks, C. S. et al. Reticular electronic tuning of porphyrin active sites in covalent organic frameworks for electrocatalytic carbon dioxide reduction. *J. Am. Chem. Soc.* **140**, 1116–1122 (2017).
18. Kornienko, N. et al. Metal–organic frameworks for electrocatalytic reduction of carbon dioxide. *J. Am. Chem. Soc.* **137**, 14129–14135 (2015).
19. Wang, C., Xie, Z., deKrafft, K. E. & Lin, W. Doping metal–organic frameworks for water oxidation, carbon dioxide reduction, and organic photocatalysis. *J. Am. Chem. Soc.* **133**, 13445–13454 (2011).
20. Verma, S., Kim, B., Jhong, H. R., Ma, S. & Kenis, P. J. A gross-margin model for defining technoeconomic benchmarks in the electroreduction of CO₂. *ChemSusChem* **9**, 1972–1979 (2016).
21. Luc, W. & Jiao, F. Nanoporous metals as electrocatalysts: state-of-the-art, opportunities, and challenges. *ACS Catal.* **7**, 5856–5861 (2017).
22. Cao, Z. et al. A molecular surface functionalization approach to tuning nanoparticle electrocatalysts for carbon dioxide reduction. *J. Am. Chem. Soc.* **138**, 8120–8125 (2016).
23. Zhang, X. et al. Highly selective and active CO₂ reduction electrocatalysts based on cobalt phthalocyanine/carbon nanotube hybrid structures. *Nat. Commun.* **8**, 14675 (2017).
24. Li, J. et al. Efficient electrocatalytic CO₂ reduction on a three-phase interface. *Nat. Catal.* **1**, 592–600 (2018).
25. Dinh, C. T. et al. CO₂ electroreduction to ethylene via hydroxide-mediated copper catalysis at an abrupt interface. *Science* **360**, 783–787 (2018).
26. De Luna, P. et al. Catalyst electro-redeposition controls morphology and oxidation state for selective carbon dioxide reduction. *Nat. Catal.* **1**, 103–110 (2018).
27. Jiang, K. et al. Metal ion cycling of Cu foil for selective C–C coupling in electrochemical CO₂ reduction. *Nat. Catal.* **1**, 111–119 (2018).
28. Kim, D., Kley, C. S., Li, Y. & Yang, P. Copper nanoparticle ensembles for selective electroreduction of CO₂ to C2–C3 products. *Proc. Natl Acad. Sci. USA* **114**, 10560–10565 (2017).
29. Mistry, H. et al. Highly selective plasma-activated copper catalysts for carbon dioxide reduction to ethylene. *Nat. Commun.* **7**, 12123 (2016).
30. Kuhl, K. P., Cave, E. R., Abram, D. N. & Jaramillo, T. F. New insights into the electrochemical reduction of carbon dioxide on metallic copper surfaces. *Energy Environ. Sci.* **5**, 7050–7059 (2012).
31. Tzeng, Y.-K. et al. Time-resolved luminescence nanothermometry with nitrogen-vacancy centers in nanodiamonds. *Nano Lett.* **15**, 3945–3952 (2015).
32. Mochalin, V. N., Shenderova, O., Ho, D. & Gogotsi, Y. The properties and applications of nanodiamonds. *Nat. Nanotechnol.* **7**, 11–23 (2012).
33. Liu, Y., Chen, S., Quan, X. & Yu, H. Efficient electrochemical reduction of carbon dioxide to acetate on nitrogen-doped nanodiamond. *J. Am. Chem. Soc.* **137**, 11631–11636 (2015).
34. Guo, D. et al. Active sites of nitrogen-doped carbon materials for oxygen reduction reaction clarified using model catalysts. *Science* **351**, 361–365 (2016).
35. Wang, H., Chen, Y., Hou, X., Ma, C. & Tan, T. Nitrogen-doped graphenes as efficient electrocatalysts for the selective reduction of carbon dioxide to formate in aqueous solution. *Green Chem.* **18**, 3250–3256 (2016).
36. Zou, Y. S. et al. Structural characterization of nitrogen doped diamond-like carbon films deposited by arc ion plating. *Appl. Surf. Sci.* **241**, 295–302 (2005).
37. Varela, A. S. et al. Metal-doped nitrogenated carbon as an efficient catalyst for direct CO₂ electroreduction to CO and hydrocarbons. *Angew. Chem. Int. Ed. Engl.* **54**, 10758–10762 (2015).
38. Song, Y. et al. High-selectivity electrochemical conversion of CO₂ to ethanol using a copper nanoparticle/N-doped graphene electrode. *ChemistrySelect* **1**, 6055–6061 (2016).
39. Peterson, A. A., Abild-Pedersen, F., Studt, F., Rossmeisl, J. & Nørskov, J. K. How copper catalyzes the electroreduction of carbon dioxide into hydrocarbon fuels. *Energy Environ. Sci.* **3**, 1311–1315 (2010).
40. Birdja, Y. Y. & Koper, M. T. The importance of cannizzaro-type reactions during electrocatalytic reduction of carbon dioxide. *J. Am. Chem. Soc.* **139**, 2030–2034 (2017).
41. Li, C. W., Ciston, J. & Kanan, M. W. Electroreduction of carbon monoxide to liquid fuel on oxide-derived nanocrystalline copper. *Nature* **508**, 504–507 (2014).
42. Bhattacharyya, S. et al. Synthesis and characterization of highly-conducting nitrogen-doped ultrananocrystalline diamond films. *Appl. Phys. Lett.* **79**, 1441–1443 (2001).
43. Henkelman, G., Arnaldsson, A. & Jónsson, H. A fast and robust algorithm for Bader decomposition of charge density. *Comput. Mater. Sci.* **36**, 354–360 (2006).
44. Liu, C. et al. Stability and effects of subsurface oxygen in oxide-derived Cu catalyst for CO₂ reduction. *J. Phys. Chem. C* **121**, 25010–25017 (2017).
45. Liu, X. et al. Understanding trends in electrochemical carbon dioxide reduction rates. *Nat. Commun.* **8**, 15438 (2017).
46. Liu, X. et al. pH effects on the electrochemical reduction of CO₍₂₎ towards C₂ products on stepped copper. *Nat. Commun.* **10**, 32 (2019).
47. Jens, K., Studt, F., Abild-Pedersen, F. & Bligaard, T. (eds) *Fundamental Concepts in Heterogeneous Catalysis* (John Wiley & Sons, 2014).
48. Cavalca, F. et al. Nature and distribution of stable subsurface oxygen in copper electrodes during electrochemical CO₂ reduction. *J. Phys. Chem. C* **121**, 25003–25009 (2017).
49. Garza, A., Bell, A. T. & Head-Gordon, M. Is subsurface oxygen necessary for the electrochemical reduction of CO₂ on copper? *J. Phys. Chem. Lett.* **9**, 601–606 (2018).
50. Yang, H. J. et al. Promoting ethylene selectivity from CO₂ electroreduction on CuO supported onto CO₂ capture materials. *ChemSusChem* **11**, 881–887 (2018).

Methods

Preparation of ND, N-ND and N-ND/Cu. The polynanocrystal diamond film seeding preparation was as follows. Due to the large amount of graphite on the surface of nanodiamond seeds, the surface was oxidized by heating in air at 500 °C for 1.5 h with carboxylation in concentrated $H_2SO_4–HNO_3$ (3:1, v/v) at 100 °C for 3 d. Through a sequence of oxidation and strong acid treatment, nanodiamond seeds were redissolved in water solution at a concentration of 1 mg ml^{-1}. Ultrasound sonication of the Si wafer with nanodiamond slurry for 30 min was adequate to achieve the highly efficient and uniform deposition of nanodiamond seeding onto the surface of the substrate. Then, the wafer was baked at 120 °C for 30 min before being placed into the CVD growth chamber. The nitrogen-doped nanodiamond films were synthesized using microwave plasma CVD (MPCVD, Seki Diamond Systems SDS 5010). The plasma was generated by microwave radiation of 2.45 GHz and the power was 1,300 W. The silicon wafer (thickness, ~550–600 μm; resistivity, ~0.001–0.005 Ωcm) was placed in the CVD chamber on a molybdenum holder. The working pressure was at 40 Torr. The flow rates of methane (CH_4), nitrogen (N_2) and hydrogen (H_2) were 10 sccm, ~0–25 sccm and 300 sccm, respectively. The molybdenum stage was heated to 540 °C and all of the growth times were 2 h. After growth, the substrate temperature was cooled down to room temperature with hydrogen gas. The copper nanoparticles were sputtered on top of the N-ND film using an AJA International Sputtering System (AJA International). The argon plasma was ignited using an external planar antenna (also known as a transformer coupled plasma antenna) connected to a (13.56 MHz) RF power generator. The substrate was placed on a movable 25-cm^2 square substrate holder and was parallel to the Cu target ($50 \times 50 \times 0.1$ mm^3). The distance between the target and the substrate was about 25 cm. The base pressure in the deposition chamber was below 2×10^{-5} Torr. A gun power of 150 W and a pressure of 15×10^{-3} Torr were used.

Material characterization. TEM characterizations were carried out using an FEI Titan 80–300 environmental (scanning) transmission electron microscope (E(S)TEM) operated at 300 kV. SEM images (FEI Magellan 400 XHR) were obtained with beam energies of 3 kV. AFM images were collected simultaneously with laser feedback from an XE-70 Park AFM. Raman spectroscopy (Horiba Labram HR Evolution Raman System) was conducted using a 532-nm excitation laser. XPS (PHI VersaProbe 3) was carried out using an Al(Kα) source. Nanoscale SIMS (NanoSIMS, CAMECA) was used for element mapping with a lateral resolution of ~200 nm. GIWAXS was conducted at beamline 7.3.3 at the Advanced Light Source, Lawrence Berkeley National Laboratory, using an approximately 0.5-mm wide 10-keV X-ray beam. The Cu K edge EXAFS was performed on beamline 11-2 at the Stanford Synchrotron Radiation Light Source using a half-tuned double Si(220) (φ = 0°) liquid N_2-cooled monochromator on unfocused beam and a 100-element Ge solid-state detector.

Preparation of N-ND/Cu cross-section TEM sample. The sample was prepared using a Ga$^+$ SEM/FIB (ThermoFisher Helios 600i) and extracted with an OmniProbe Autoprobe 200 micromanipulator. The sample was protected by layers of Pt deposited in situ with the electron and ion beams. Final thinning to electron transparency was accomplished with an 8-kV ion beam.

Electrochemical measurements. The electrochemical measurements were carried out in a gas-tight, two-compartment electrochemical cell system controlled with a VMP3 multichannel electrochemical workstation (Biologic), with a Pt foil as the counter electrode and Ag/AgCl as the reference electrode. The two compartments separate the working and counter electrodes with an anion exchange membrane. Each compartment holds 20 ml of the electrolyte and the working compartment was sealed to allow measurements of gaseous products. The electrocatalytic reduction of CO_2 was conducted in a CO_2-saturated 0.5 M KHCO$_3$ solution (pH 7.3) at room temperature and under atmospheric pressure. After CO_2 was purged into the KHCO$_3$ solution for at least 30 min to remove residual air in the reservoir, controlled potential electrolysis was performed at each potential for 4 h. The oxygen generated at the anode was vented out of the reservoir. The ECSAs for the electrodes were determined by double-layer capacitance measurements[51].

CO_2 reduction electrolysis and product analysis. The gas products of the CO_2 electrocatalytic reduction were monitored using an online multiple gas analyser 8610C GC system equipped with a Haysep-D column (1/8 inch × 6 ft) and a 13× Mol Sieve column (1/8 inch × 6 ft) (SRI Instruments). Ethanol, acetate, formate and methanol concentrations were analysed on a Varian Inova 600-MHz NMR spectrometer. A 0.5-ml sample of the electrolyte was mixed with 0.1 ml D$_2$O and 1.67 ppm (by mass fraction) dimethyl sulfoxide was added as an internal standard. LSV scans were also recorded in CO_2-saturated 0.5 M KHCO$_3$ (pH 7.3). All potentials in this study were measured against the Ag/AgCl reference electrode and converted to the RHE reference scale by E (versus RHE) = E (versus Ag/AgCl) + 0.21 V + 0.0591 × pH.

DFT calculations. All the calculations were carried out with DFT implanted in Quantum ESPRESSO[52], using plane-wave basis set[53] and ultrasoft pseudopotential[54,55], interfaced with the atomic simulation environment[56].

Plane-wave and density cut-offs of 500 eV and 5,000 eV were used with BEEF-vdW (ref. [57]) exchange-correlation functional. The $(12 \times 12 \times 1)$, $(6 \times 61 \times 1)$ and $(2 \times 6 \times 1)$ Monkhorst–Pack[58] grid K-points were used, respectively, for (1×1), (2×2), (3×3) and (6×2) surface supercells, all with a vacuum layer of 14 Å. The diamond(111) surface was described by a three bilayer slab with the bottom two layers fixed. The dangling bonds of the bare surface were saturated by H atoms. Dipole corrections were applied in the z direction[59]. The structures were relaxed until the maximal force on the atoms was smaller than -0.05 eV Å^{-1}. The charge on the atoms was obtained via a Bader analysis[43,60]. Transition states were determined using the nudged elastic band method with climbing image[61,62]. The computational hydrogen electrode[63] model was applied to calculate the chemical potential of proton–electron pairs at any potential using the following:

$$\mu_{H^+} + \mu_{e^-} = 1/2\mu_{H_2}^o - eU \qquad (2)$$

where U is the potential versus RHE, and $\mu_{H_2}^o$ is the chemical potential of H_2 gas under standard conditions. The adsorption energies of the reaction intermediates were calculated as:

$$E_f\left(X^*\right) = E(X^*) - E(^*) - \sum_i n_i\mu_i \qquad (3)$$

where $E(X^*)$ is the energy of the adsorbate on the substrate, $E(^*)$ the energy of the bare substrate, n_i the number of atom i in the adsorbate and μ_i the chemical potential of atom i. Under CO_2 reduction conditions, we define:

$$\mu_H = \frac{1}{2}E_{H_2} \qquad (4)$$

$$\mu_O = E_{H_2O} - 2\mu_H \qquad (5)$$

$$\mu_C = E_{CO_2} - 2\mu_O \qquad (6)$$

and adsorption free energies G_f were obtained by including the zero-point energy, enthalpy and entropy correction of the adsorbate and the gas species[45].

Data availability

The data that support the plots within this paper and other findings of this study are available from the corresponding author on reasonable request.

References

51. Waszczuk, P., Zelenay, P. & Sobkowski, J. Surface interaction of benzoic-acid with a copper electrode. *Electrochim. Acta* **40**, 1717–1721 (1995).
52. Giannozzi, P. et al. QUANTUM ESPRESSO: a modular and open-source software project for quantum simulations of materials. *J. Phys. Condens. Matter* **21**, 395502 (2009).
53. Kresse, G. & Furthmüller, J. Efficiency of ab-initio total energy calculations for metals and semiconductors using a plane-wave basis set. *Comput. Mater. Sci.* **6**, 15–50 (1996).
54. Kresse, G. & Hafner, J. Norm-conserving and ultrasoft pseudopotentials for first-row and transition elements. *J. Phys. Condens. Matter* **6**, 8245 (1994).
55. Vanderbilt, D. Soft self-consistent pseudopotentials in a generalized eigenvalue formalism. *Phys. Rev. B* **41**, 7892–7895 (1990).
56. Bahn, S. R. & Jacobsen, K. W. An object-oriented scripting interface to a legacy electronic structure code. *Comput. Sci. Eng.* **4**, 56–66 (2002).
57. Wellendorff, J. et al. Density functionals for surface science: exchange-correlation model development with Bayesian error estimation. *Phys. Rev. B* **85**, 235149 (2012).
58. Monkhorst, H. J. & Pack, J. D. Special points for Brillouin-zone integrations. *Phys. Rev. B* **13**, 5188–5192 (1976).
59. Bengtsson, L. Dipole correction for surface supercell calculations. *Phys. Rev. B* **59**, 12301–12304 (1999).
60. Tang, W., Sanville, E. & Henkelman, G. A grid-based bader analysis algorithm without lattice bias. *J. Phys. Condens. Matter* **21**, 084204 (2009).
61. Henkelman, G., Uberuaga, B. P. & Jónsson, H. A climbing image nudged elastic band method for finding saddle points and minimum energy paths. *J. Chem. Phys.* **113**, 9901–9904 (2000).
62. Henkelman, G. & Jónsson, H. Improved tangent estimate in the nudged elastic band method for finding minimum energy paths and saddle points. *J. Chem. Phys.* **113**, 9978–9985 (2000).
63. Nørskov, J. K. et al. Origin of the overpotential for oxygen reduction at a fuel-cell cathode. *J. Phys. Chem. B* **108**, 17886–17892 (2004).

Author contributions

H.W., Y.-K.T., S.C. and Y.C. conceived the research. H.W. and Y.-K.T. carried out the synthesis and performed materials characterization and electrochemical measurements. Y.Li, J.L., X.Zheng, A.Y., Y.Liu, Y.G., L.C., Yu.Li, X.Zhang, W.C., B.L., H.L., N.A.M. and Z.-X.S. assisted in the synthesis and characterization of materials. Y.J. and K.C. carried out the theoretical calculation. H.W., Y.-K.T., Y.J., K.C. and Y.C. analysed the data. H.W., Y.-K.T., Y.J., K.C., T.T., S.C. and Y.C. wrote the paper.

Competing interests

The authors declare no competing interests.

Additional information

Supplementary information is available for this paper at https://doi.org/10.1038/s41565-019-0603-y.

Correspondence and requests for materials should be addressed to K.C., T.T., S.C. or Y.C.

Peer review information *Nature Nanotechnology* thanks Antonio Martin and other, anonymous, reviewer(s) for their contribution to the peer review of this work.

Reprints and permissions information is available at www.nature.com/reprints.